Acoust. Sci. & Tech. **28**, 6 (2007)

PAPER

Effects of the false vocal folds on sound generation by an unsteady glottal jet through rigid wall model of the larynx

Hideyuki Nomura* and Tetsuo Funada

Division of Electrical Engineering and Computer Science, Kanazawa University, Kakuma-machi, Kanazawa, 920–1192 Japan

(*Received 3 February 2007, Accepted for publication 18 May 2007*)

Abstract: In the present paper, the effects of the false vocal folds (FVFs) on sound generation induced by an unsteady glottal jet through a two-dimensional rigid wall model of the larynx are investigated by conducting numerical experiments. The glottal jets are simulated by solving the basic equations for a compressible viscous fluid based on the larynx model with and without the FVFs. The existence of the FVFs increases the amplitude of noise-like pressure fluctuation at the glottis and faraway from the glottis. Furthermore, the FVFs give rise to the broadbanding of the pressure spectrum throughout the fluid domain. These results indicate that the FVFs have a profound effect on the generation of broadband noise components in a speech wave.

Keywords: Glottal jet, Rigid wall model of the larynx, False vocal folds, Sound generation, Numerical simulation

PACS number: 43.70.Aj, 43.70.Bk, 43.28.Ra [doi:10.1250/ast.28.403]

1. INTRODUCTION

With improvements in computing power, numerical simulation has become an efficient tool for clarifying the speech production process. A two-mass model developed by Ishizaka and Flanagan [1] and improved models [2,3] based on this model are the most popular numerical models for speech production. These models can be used to describe the principal mechanism of phonation, although the structure of the model is simple. However, these models are not suitable for the description of complex phenomena [4–7] in the larynx, because these models have a limitation with respect to the degree of freedom of fluid motion in the larynx and do not provide accurate glottis shapes.

During any vibration cycle of the true vocal folds (TVFs), the glottis takes on converging, uniform, and diverging shapes. Numerical simulations conducted by Iijima *et al.* [8] and Liljencrants [9] revealed that the pressure distributions on the glottal surface are greatly affected by both the shape and minimal diameter of the glottis. Although asymmetric flows similar to that observed via measurements [10] were obtained in their simulation, Iijima *et al.* conjectured that the asymmetry was due to numerical errors in computation.

*e-mail: nomu@t.kanazawa-u.ac.jp

In a previous study [11], we numerically simulated glottal flows on the basis of a two-dimensional rigid wall model of the larynx and reported that rather than being a steady symmetric laminar flow, the glottal flow is an unsteady asymmetric flow similar to the physically measured flows. In addition, the results suggest that the existence of the false vocal folds (FVFs) increases the intensity of the sound due to an unsteady flow. However, the mechanism of the increase in the intensity has not been investigated in detail.

Zhang *et al.* [12] numerically investigated the effect of the FVFs on the speech production process on the basis of the axisymmetric forced vibrating TVF model. They reported that the impingement of the glottal jet on the FVFs causes the generation of additional sources in speech waves. However, we infer that they underestimated the effects of the existence of the FVFs on the speech waves, because, in the axisymmetric model, the degree of freedom of the fluid motion was limited, and the glottal flow could not be transformed into an asymmetric complicated flow.

The purpose of the present study is to investigate the effects of the FVFs on the speech production process. As a first step, we do not consider the interaction between the glottal flow and vibrating TVFs, because our only focus is on the effect of the FVFs on sound generation caused by an unsteady flow. In the present study, we conduct a numerical experiment with glottal jets on two-dimensional

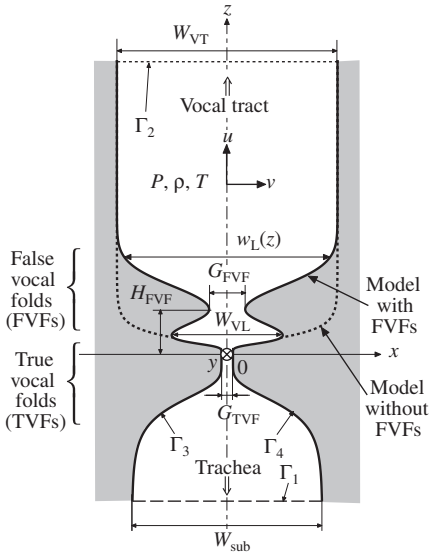

Fig. 1 Analytical model for the glottal flow in the coronal (z-x) plane. Bold solid and dotted lines indicate the model with the false vocal folds (FVFs) and the model without the FVFs and the ventricle of the larynx, respectively. The configuration is assumed to be uniform in the sagittal (y) direction. The function of larynx width is described by the function $w_L(z)$ in the Appendix.

rigid larynx models with and without the FVFs at different lung pressures. The effects of the FVFs on the sound generation within the larynx, especially on the amplitude and spectrum slope thereof, are discussed quantitatively. Furthermore, we show two types of mechanism of sound generation induced by unsteady glottal flow.

2. ANALYTICAL MODEL AND COMPUTATIONAL METHODS

A real larynx has a complex three-dimensional shape. The main simplification of the present study is to consider the flow to be a two-dimensional configuration. This precludes the vortex stretching mechanism, that causes the energy cascade from larger to smaller scale vortices [13]. Therefore, in the present simulation, large-scale vortices tend to remain in the flow field.

2.1. Larynx Model and Governing Equations

A two-dimensional model of the larynx without vibration in the coronal (z-x) plane is shown in Fig. 1. The bold solid and dotted lines indicate models with and without the FVFs, respectively. The configuration is symmetric about the center line (dot-dashed line, i.e., the z axis). The large ratio of the TVF length of $\mathcal{O}(10^1)$ mm to the the TVF gap of $\mathcal{O}(10^0)$ mm allows the flow configuration in the sagittal (y) direction to be uniform; that is, $\partial Q/\partial y = 0$ is assumed, where Q is a physical quantity of the flow.

Table 1 Size parameters for the larynx (values are in mm).

W_{sub}	Width of subglottal region	16.4
W_{VL}	Width of ventricle of the larynx	10.3
W_{VT}	Width of vocal tract	20.0
G_{TVF}	True vocal fold gap	1.0
G_{FVF}	False vocal fold gap	5.1
H_{FVF}	False vocal fold height	6.2

The size parameters of the larynx presented in Table 1 are based on the data reported by Scherer *et al.* [14]. In the present study, we consider only a simple uniform parallel glottis model with a TVF gap of $G_{TVF} = 1$ mm, although the glottal angle affects the glottal jet [5,10,11,15]. The function of larynx width is described by the function $w_L(z)$ in the Appendix. In addition, the vocal tract configuration is assumed to be a uniform duct in order to highlight the acoustic and fluid phenomena within the larynx.

In the present paper, all variables denoted by the superscript * are nondimensional values. In order to formulate the problems, we introduce the following dimensionless variables:

$$\left.\begin{aligned} t^* = \frac{c_0 t}{L},\ z^* = \frac{z}{L},\ x^* = \frac{x}{L}, \\ u^* = \frac{u}{c_0},\ v^* = \frac{v}{c_0},\ P^* = \frac{P}{\rho_0 {c_0}^2},\ T^* = \frac{T}{T_0}, \end{aligned}\right\} \quad (1)$$

where t is the time, u and v indicate the z and x components, respectively, of the flow velocity vector $\boldsymbol{u}$, $P = p + P_{atm}$ is the total pressure (p is the pressure variation from the atmospheric pressure value P_{atm}), ρ is the density of the medium, T is the absolute temperature, $L = W_{VT}$ (=20 mm) is the characteristic length, ρ_0 (= 1.138 kg/m^3) is the fluid density at rest, and c_0 (= 3.532×10^2 m/s) is the sound velocity of infinitesimal amplitude. The variables denoted by the subscript $_0$ are quantities at an atmospheric pressure P_{atm} of 101.3 kPa and a temperature of 310.15 K (=T_0, 37°C).

Because of the complexity of the boundary shape in the larynx, the Cartesian coordinates (z^*, x^*) are transformed into general curvilinear coordinates (ξ^*, η^*) along the laryngeal surface. The basic governing equations of a compressible viscous fluid like the glottal flow in a two-dimensional space are summarized in the following compact form [11,16]:

$$\frac{\partial \boldsymbol{Q}^*}{\partial t^*} + \frac{\partial \boldsymbol{E}^*}{\partial \xi^*} + \frac{\partial \boldsymbol{F}^*}{\partial \eta^*} = \frac{1}{Re}\left(\frac{\partial \boldsymbol{R}^*}{\partial \xi^*} + \frac{\partial \boldsymbol{S}^*}{\partial \eta^*}\right), \quad (2)$$

where Re (= $\rho_0 c_0 L/\mu_0$) is the Reynolds number, and μ_0 (= 1.902×10^{-5} Pa·s) is the shear viscosity. Other dependent variable vectors for the flow are expressed as follows:

$$\boldsymbol{Q}^* = \frac{1}{J^*}\begin{bmatrix} \rho^* \\ \rho^* u^* \\ \rho^* v^* \\ e^* \end{bmatrix}, \tag{3}$$

$$\boldsymbol{E}^* = \frac{1}{J^*}\begin{bmatrix} \rho^* U^* \\ \rho^* u^* U^* + \xi_x^* P^* \\ \rho^* v^* U^* + \xi_y^* P^* \\ (e^* + P^*)U^* \end{bmatrix}, \quad \boldsymbol{F}^* = \frac{1}{J^*}\begin{bmatrix} \rho^* V^* \\ \rho^* u^* V^* + \eta_z^* P^* \\ \rho^* v^* V^* + \eta_x^* P^* \\ (e^* + P^*)V^* \end{bmatrix}, \tag{4}$$

$$\boldsymbol{R}^* = \frac{1}{J^*}\begin{bmatrix} 0 \\ \xi_z^* \tau_{zz}^* + \xi_x^* \tau_{zx}^* \\ \xi_z^* \tau_{xz}^* + \xi_x^* \tau_{xx}^* \\ \xi_z^* R_4^* + \xi_x^* S_4^* \end{bmatrix}, \quad \boldsymbol{S}^* = \frac{1}{J^*}\begin{bmatrix} 0 \\ \eta_z^* \tau_{zz}^* + \eta_x^* \tau_{zx}^* \\ \eta_z^* \tau_{xz}^* + \eta_x^* \tau_{xx}^* \\ \eta_z^* R_4^* + \eta_x^* S_4^* \end{bmatrix}. \tag{5}$$

Here,

$$\left.\begin{aligned} R_4^* &= \tau_{zz}^* u^* + \tau_{zx}^* v^* + q_z^*, \\ S_4^* &= \tau_{xz}^* u^* + \tau_{xx}^* v^* + q_x^*. \end{aligned}\right\} \tag{6}$$

U^* and V^* are contravariant velocity components in the ξ^* and η^* directions, respectively, and are written as

$$\left.\begin{aligned} U^* &= \xi_z^* u^* + \xi_x^* v^*, \\ V^* &= \eta_z^* u^* + \eta_x^* v^*. \end{aligned}\right\} \tag{7}$$

J^* is the Jacobian of the coordinate transformation, and ξ_z^*, ξ_x^*, η_z^*, and η_x^* are the components of the transformation matrix $\partial(\xi^*, \eta^*)/\partial(z^*, x^*)$. In addition, τ_{zz}^*, τ_{xx}^*, and $\tau_{zx}^* = \tau_{xz}^*$ are the dimensionless viscosity-induced drag forces, and q_z^* and q_x^* are the dimensionless heat fluxes.

The dimensionless total energy density is given as

$$e^* = \frac{P^*}{\gamma - 1} + \frac{1}{2}\rho^*\left(u^{*2} + v^{*2}\right), \tag{8}$$

where γ (= 1.403) is the specific heat ratio. In addition, an adiabatic relationship for a compressible fluid is used to connect the absolute temperature and the pressure, as follows:

$$P^* = \frac{\rho^* T^*}{\gamma}. \tag{9}$$

2.2. Numerical Simulation

In order to solve these nonlinear partial differential equations, we employ a numerical computation method, MacCormack's finite difference scheme, which has fourth-order accuracy with respect to space and second-order accuracy with respect to time [17]. The computational domain extends from $z^* = -8$ to $z^* = 10$, i.e., $z = -160 \sim 200$ mm. The grid number is 800×120. A greater grid number is necessary in computations in order to obtain an accurate solution. However, we reached a compromise between numerical accuracy and computational time [11].

The dimensions of the grid in the z^* direction are reduced near the glottis at $z^* = 0$, and the dimensions of the grid in the x^* direction are regular. Here, the minimum grid sizes become $\Delta z \simeq 40\,\mu$m and $\Delta x \simeq 8\,\mu$m.

The time is discretized at an interval of $\Delta t \simeq 0.1\,\mu$s. The Courant-Friedrichs-Levy condition [16] for numerical convergence of the difference equations is satisfied because the CFL number becomes 0.6, which is less than unity. Calculated data are written to output files at intervals of 10 μs.

The details of the analysis are found in the previous paper [11].

2.3. Initial and Boundary Conditions

Suppose that the air in the entire fluid space is uniform and at rest for $t^* \le 0$. The initial conditions are then readily obtained for the entire space:

$$|\boldsymbol{u}^*| = 0, \quad \rho^* = 1, \quad P^* = 1/\gamma \quad \text{for} \quad t^* \le 0. \tag{10}$$

Nonslip and adiabatic boundary conditions are specified on the boundaries Γ_3 and Γ_4 in Fig. 1. A nonreflecting characteristic boundary condition [18] is imposed at the outflow boundary Γ_2 in order to minimize acoustic reflection. A pressure function $P_{\text{in}}^*(t^*) = p_{\text{L}}^*(t^*) + 1/\gamma$ is applied to the boundary Γ_1, where $p_{\text{L}}^*(t^*)$ is the lung pressure,

$$p_{\text{L}}^*(t^*) = \begin{cases} \dfrac{P_{\text{L0}}^*}{2}\left\{1 - \cos\left(\dfrac{\pi t^*}{t_{\text{r}}^*}\right)\right\} & \text{for } 0 < t^* \le t_{\text{r}}^*, \\ P_{\text{L0}}^* & \text{for } t^* > t_{\text{r}}^*. \end{cases} \tag{11}$$

Here, $P_{\text{L0}}^* (= P_{\text{L0}}/(\rho_0 {c_0}^2))$ and $t_{\text{r}}^* (= c_0 t_{\text{r}}/L)$ are the steady state value of the lung pressure and the time required for the lung pressure to increase to P_{L0}^* from atmospheric pressure, respectively. In the present paper, the rise time t_{r} is set to a constant value of 10 ms.

3. RESULTS AND DISCUSSION

In order to gain insight into the effects of the FVFs on sound generation induced by unsteady glottal jets, the jets based on the two-dimensional model of the larynx with and without FVFs are numerically simulated by varying the lung pressure P_{L0}. We first show the effects of the FVFs on the amplitude of the sound caused by the unsteady glottal jet, and then show the effects on the spectrum thereof.

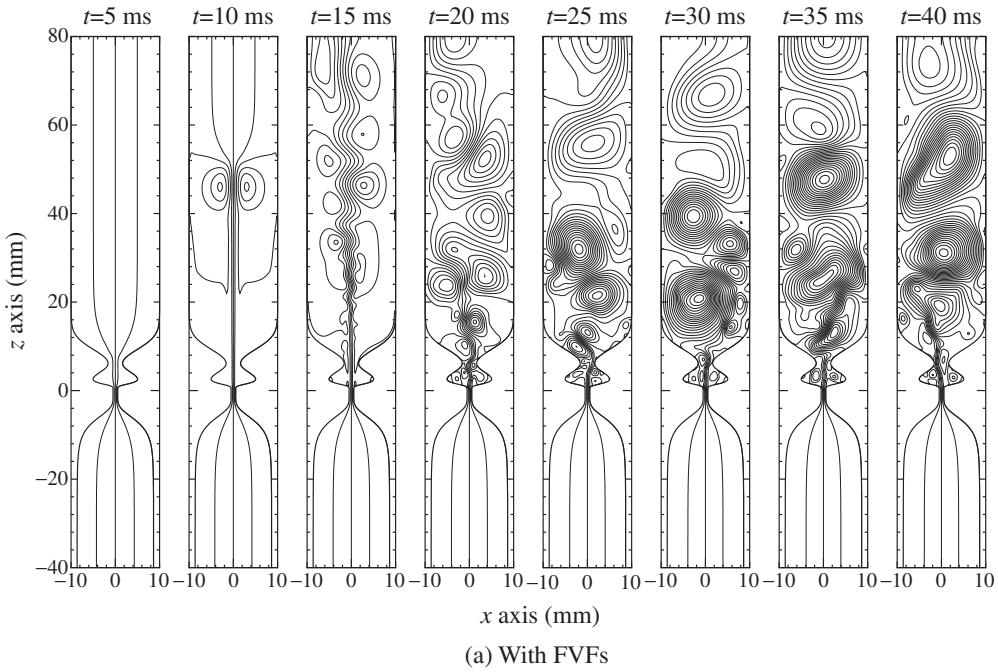

(a) With FVFs

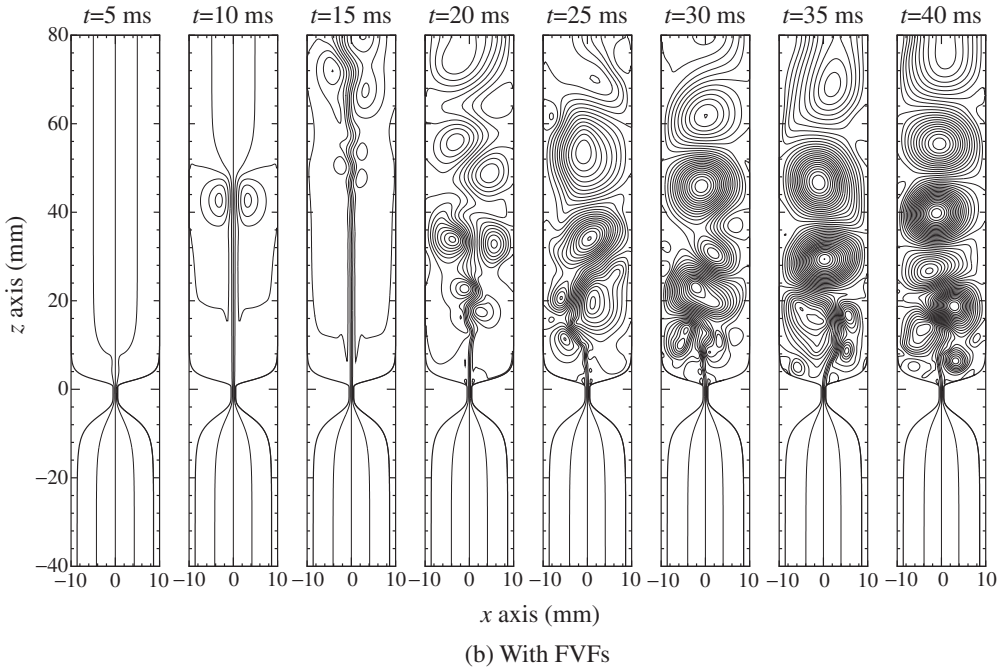

(b) With FVFs

Fig. 2 Time sequences of instantaneous streamline patterns of the glottal flow at $P_{L0} = 800\,\text{Pa}$.

3.1. Glottal Jet Distribution in the Larynx

Figure 2 shows the time sequences of instantaneous streamline patterns of two-dimensional glottal flows based on the models with and without the FVFs at every 5 ms. The lung pressure P_{L0} is set at 800 Pa, which corresponds to the value for an ordinary conversation level. In both models, symmetric jets about the z axis are first ejected from the glottis, and the symmetries of the jets are then broken for each jet front. Finally, the flow changes into an unsteady pattern with several vortices.

The flows at $t = 40\,\text{ms}$ in Fig. 2 near the glottis are shown in Fig. 3 with expanded coordinates. In the model with the FVFs, the impingement of the glottal jet on the FVFs and small vortices within the ventricle of the larynx are observed.

3.2. Sound Generation Induced by Unsteady Glottal Flow

Figure 4 shows the instantaneous pressure $p(t) = P(t) - P_{\text{atm}}$ at different distances from the glottis. These sound waves are directly obtained by numerical simulations without any acoustic analogy.

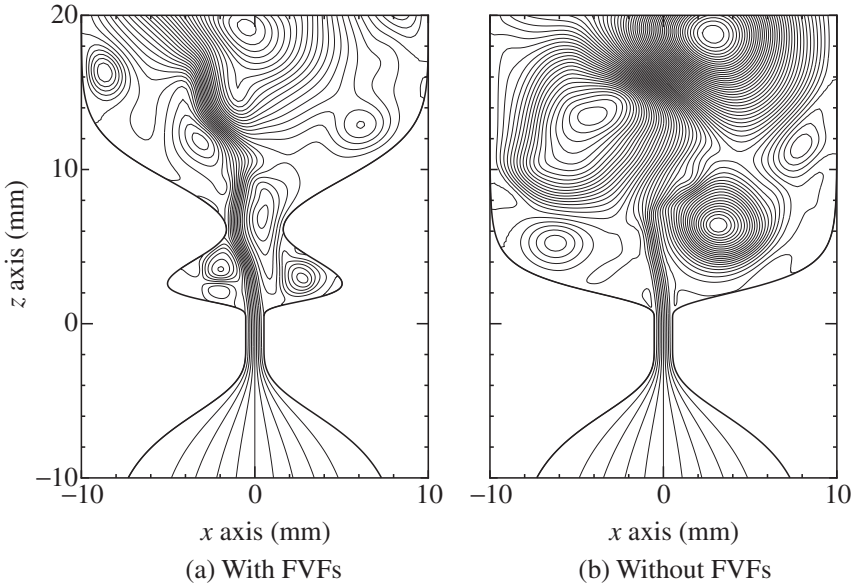

Fig. 3 Instantaneous streamline of the glottal flow near the glottis for $P_{L0} = 800\,\text{Pa}$ at $t = 40\,\text{ms}$. The flow is identical to that shown in Fig. 2 at $t = 40\,\text{ms}$ (shown with expanded coordinates).

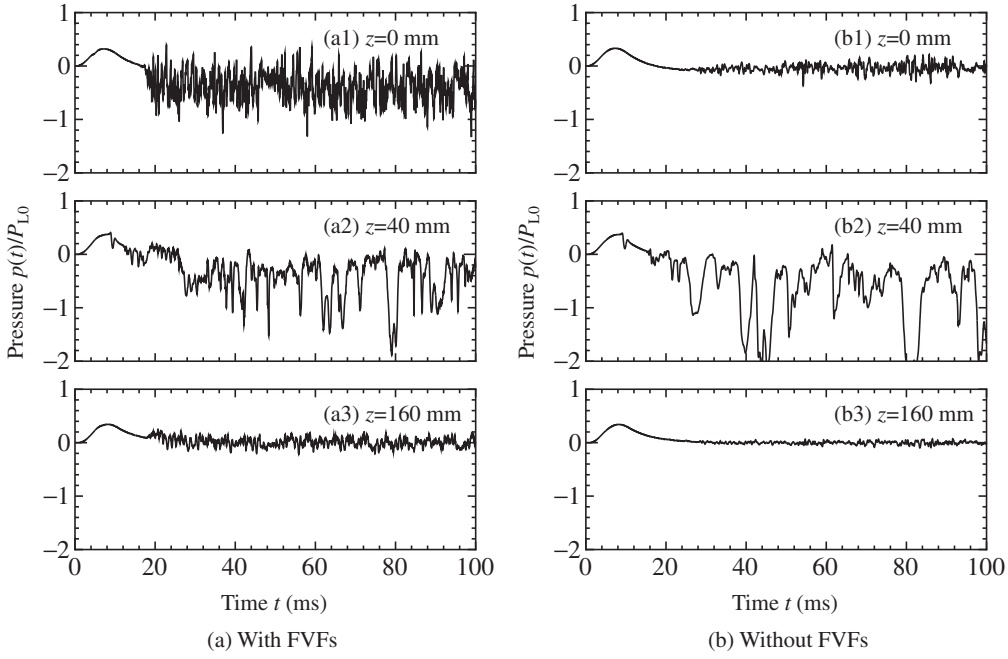

Fig. 4 Instantaneous pressure $p(t) = P(t) - P_{atm}$ in the glottal flow for $P_{L0} = 800\,\text{Pa}$.

At $z = 0\,\text{mm}$, the amplitude (peak-to-peak) of pressure variation in the model with the FVFs is approximately 1 in Fig. 4(a1), and that in the model without the FVFs is approximately 0.4 in Fig. 4(b1). The pressure amplitude in the model without the FVFs is in rough agreement that according to the measured data based on a rigid model having a lip like glottis without FVFs reported by Hofmans *et al.* [5].

In the region downstream of the FVFs, both amplitudes (peak-to-peak) of the pressure variation are approximately 2 in Figs. 4(a2) and (b2).

It is difficult to obtain radiated sounds from the mouth, since the effects of acoustic loading of the vocal tract and the mouth in the present simulation are ignored. Instead, the sound within the vocal tract at a distance faraway from the glottis $z = 160\,\text{mm}$ are shown in Figs. 4(a3) and (b3). The amplitude in the model with the FVFs is about twice that in the model without the FVFs.

The unsteady glottal flow causes pressure fluctuation within the larynx. The pressure wave $p(t)$ shows a fluctuation, $p'(t)$, around the average component $\langle p \rangle$, where the notation $\langle \quad \rangle$ denotes a time averaging operator.

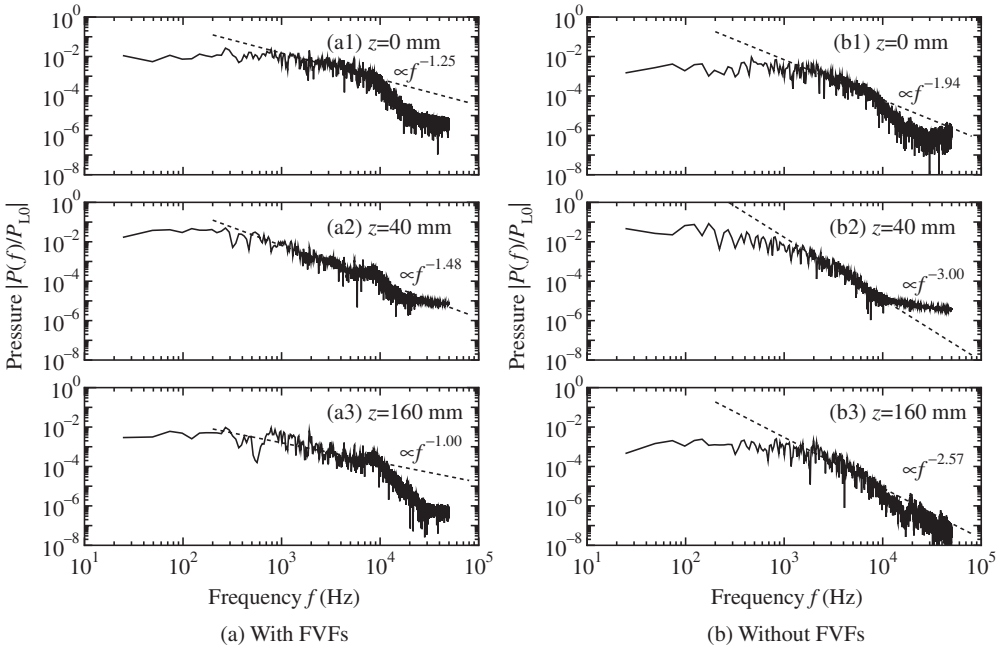

Fig. 5 Frequency spectra of pressure in the unsteady glottal flow at $P_{L0} = 800$ Pa. These results correspond to the pressure in Fig. 4. The dashed curves are fitting curves using a function $|P(f)| \propto f^{-\alpha}$ with α ranging from 1 kHz to 10 kHz.

We can write an expression for the instantaneous pressure as

$$p(t) = \langle p \rangle + p'(t). \tag{12}$$

The average pressure $\langle p \rangle$ at the glottis corresponds to Bernoulli's pressure, which indicates negative pressure due to high-speed flow through a constriction. Theoretical and measured Bernoulli's pressures (the maximum average pressure drops in the glottis) are of the order of $-0.1P_{L0}$ in the model without the FVFs based on a steady flow assumption [1,5,19]. In the present simulation, Bernoulli's pressures at $z = 0$ mm in the models with and without the FVFs are $-0.4P_{L0}$ and $-0.05P_{L0}$, respectively. The reasons why the Bernoulli's pressure in the model without the FVFs is somewhat lower than the pressures in the theory and measurements are that the value of intraglottal pressure depends on the measured location within the glottis [19], and that the pressure measured at $z = 0$ mm in this model is not the maximum value. On the other hand, the Bernoulli's pressure of this simulation in the model with the FVFs is four times higher than the theoretical and measured pressures. This large Bernoulli's pressure is most likely due to an effect of vortex motions within the ventricle of the larynx. This effect will be discussed in Sect. 3.3.

Figure 5 shows the normalized pressure spectra $P(f)/P_{L0}$, where f is the frequency. The spectra are obtained by performing an FFT analysis on the pressure fluctuation sampled at 100 kHz in the range of 60 to 100 ms. The dashed curves indicate the fitting curves obtained using a function of the frequency f with exponent α:

$$\left|P(f)\right| \propto f^{-\alpha}, \tag{13}$$

in the frequency range of 1 kHz to 10 kHz.

The pressure spectra roughly decrease with increasing frequency. The slopes in the model with the FVFs are less steep than those in the model without the FVFs. In addition, both slopes in the region downstream of the FVFs $z = 40$ mm in the model with and without the FVFs are more tilted than those at the glottis. In the model with the FVFs, the slope faraway from the glottis is less steep than that at the glottis, whereas, in the model without the FVFs, the slope faraway from the glottis is greater than that at the glottis.

3.3. Amplitude of Pressure Fluctuation

The lung pressure dependence of the amplitude of the pressure fluctuation

$$P_{\mathrm{rms}} = \sqrt{\langle p'^2(t) \rangle}, \tag{14}$$

is shown in Fig. 6. Both the amplitudes at the glottis $z = 0$ mm and in the region downstream of the FVFs $z = 40$ mm exhibit a rapid increase, reaching a value of $\mathcal{O}(10^{-2}) \sim \mathcal{O}(10^{-1})$ from $\mathcal{O}(10^{-3})$ above 100 Pa in lung pressure.

In the region downstream of the FVFs at $z = 40$ mm in Fig. 6(b), both the amplitudes of pressure fluctuation in the models with and without the FVFs have the same order of magnitude. On the other hand, at the glottis ($z = 0$ mm) and faraway from the glottis ($z = 160$ mm), the amplitude in the model with the FVFs is one order of magnitude larger than that in the model without the FVFs in Figs. 6(a) and

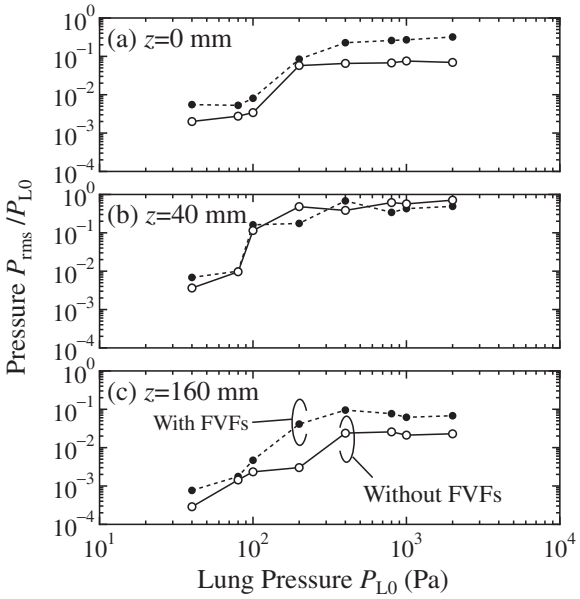

Fig. 6 Root-mean-square of the pressure fluctuation P_{rms} with respect to the lung pressure P_{L0}.

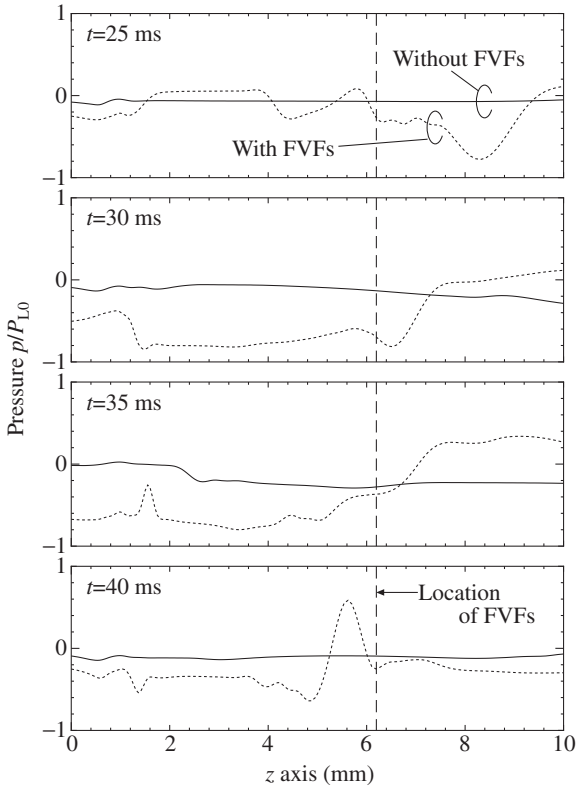

Fig. 7 Instantaneous pressure distribution on the surface of the larynx Γ_3 at $P_{L0} = 800$ Pa.

(c). These results suggest that the addition of the FVFs increases the amplitude of the pressure fluctuation within the larynx and the vocal tract except in the region downstream of the FVFs.

The impingement of the glottal jet on the FVFs and small vortices within the ventricle of the larynx have been observed in the model with the FVFs, although such vortices are not generated in the model without the FVFs, as shown in Fig. 3. Figure 7 shows the time sequence of the instantaneous pressure distribution on the laryngeal surface Γ_3 at 800 Pa. The pressure at the FVFs ($z \simeq 6$ mm) varies with time in the model with the FVFs, whereas the pressure is almost uniform and shows no change in the model without the FVFs.

In aeroacoustics, boundary layers are formed near the surface of obstacles in a flow field, and the time variation of pressure within the boundary layer causes sound sources that are related to dipole sources [20]. Therefore, the increase in the amplitude of the pressure fluctuation at the glottis caused by the existence of the FVFs is due principally to the interaction between the flow and the edges of the FVFs. The fluctuations caused by the interactions of the flow with the edges of the FVFs propagate downstream of the glottis. The increase in the pressure amplitude faraway from the glottis can be explained in terms of these propagations.

The instantaneous negative pressure of -2 at $z = 40$ mm and $t = 40$ ms in the model without the FVFs in Fig. 4(b2) is a consequence of the motion of the vortex at $z \simeq 40$ mm and $t = 40$ ms in Fig. 2(b). The large-amplitude pressure fluctuations observed downstream of the FVFs are caused by the passages of vortices for a high Reynolds number [11].

The Reynolds number determines an unsteady vortex structure. We estimated the Reynolds number with the maximum velocity within the glottis as the characteristic velocity. The Reynolds numbers in the model with and without the FVFs were nearly identical. The same amplitude levels of the pressure fluctuation at $z = 40$ mm in both of the models in Fig. 6(b) can be explained in terms of agreement with the Reynolds numbers.

The propagation wave caused by the interaction between the flow and the FVFs affects the amplitudes at the glottis ($z = 0$ mm) and faraway from the glottis ($z = 160$ mm). However, the wave amplitude at $z = 20$ mm is not greatly affected by the wave caused by the interaction between the flow and the FVFs, since the magnitude of the pressure due to the passages of vortices is larger than that due to the interaction between the flow and the FVFs.

3.4. Broadband Spectrum of Pressure Fluctuation

The lung pressure dependence of the spectral slope, $20 \log 2^{\alpha}$ (dB/oct), in the range of 1 kHz to 10 kHz based on Eq. (13) is shown in Fig. 8. The spectral slopes tend to increase as the lung pressure exceeds 100 Pa, and then decrease gradually with the lung pressure. The slopes in the model with the FVFs are less steep than that in the model

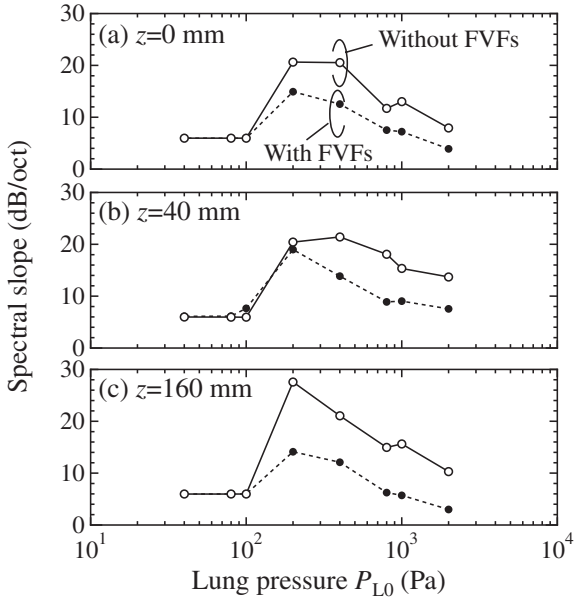

Fig. 8 Spectral slope, $20 \log 2^{\alpha}$, of pressure fluctuation in the range of 1 kHz to 10 kHz based on Eq. (13).

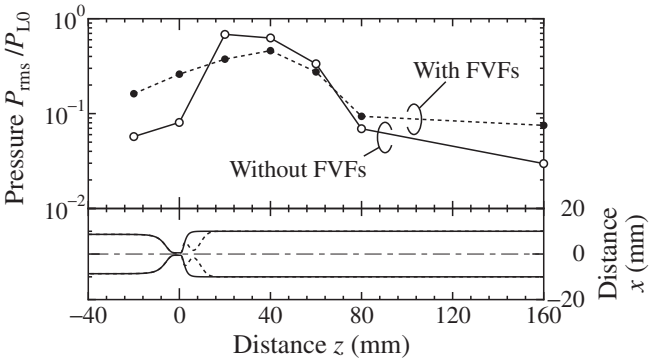

Fig. 9 Pressure distribution along the z axis at $P_{L0} = 800$ Pa.

without the FVFs. This indicates that the FVFs give rise to the broadbanding of the pressure spectrum.

Sound pressure levels at a constriction in physical models of speech production organs have been reported to decrease at a rate of roughly 8 dB/oct [21]. The physically measured slope is in reasonable agreement with that obtained by the present numerical experiment at a lung pressure of approximately 1,000 Pa with the FVFs.

We have indicated earlier that the interaction of the glottal flow with the edges of the FVFs increased the level of high frequency pressure fluctuation in Fig. 4. Therefore, it seems reasonable to conclude that the broadbanding of the pressure spectrum is also caused by the interaction between the flow and the FVFs.

3.5. Distribution of Pressure Amplitude

As mentioned above, there are two types of mechanisms for the generation of pressure fluctuation induced by unsteady flow within the rigid larynx model. One is the interaction of the flow with the FVFs, which causes broadband pressure fluctuations, and the other is the passages of vortices which cause negative large-amplitude pressure.

The distributions of the amplitude of the composite pressure fluctuation caused by these mechanisms along the z axis at $P_{L0} = 800$ Pa are shown in Fig. 9. The pressure amplitude first increases, and then decreases with the distance from the glottis. The passages of vortices cause large negative pressure. A peak at $z \simeq 40$ mm is caused by this mechanism. Since the vortices dissipate rapidly with the distance from the glottis [11], the amplitude decreases faraway from the glottis.

The broadband pressure fluctuation caused by the interaction of the flow with the edges of the FVFs propagates downstream and upstream of the glottis. The increases in pressure amplitude caused by the addition of the FVFs in the region for $z > 80$ mm and $z < 0$ mm can be explained in terms of these propagations.

We note that, with the existence of the FVFs, the amplitudes of pressure fluctuation increased, but the energy within the larynx was not amplified. In fact, both energies in the models with and without the FVFs, which are estimated by the integral of squared pressure amplitude along the z axis, were in agreement with each other.

3.6. Effect of Two-dimensional Assumption on Glottal Flow

In the present study based on the two-dimensional flow model, large-scale vortices tend to remain in the field, since the energy cascade is restricted [13]. Relatively large scale vortices downstream of the FVFs as shown in Fig. 2 are probably related to this artifact. The large pressure amplitudes in the region downstream of the FVFs, as shown in Figs. 4, 6, and 9, are affected by this fluid motion. In a three-dimensional model and a real larynx, smaller amplitudes of pressure fluctuation will probably be observed.

Pressure fluctuations with a small amplitude and a high frequency component are not greatly affected by this artifact, since similar fluctuations were measured in a physical model [5].

4. CONCLUSION

In the present study, we have performed numerical experiments on the glottal flow on the basis of two-dimensional rigid wall models of the larynx with and without the FVFs in order to examine the effects of the FVFs on the sound generation induced by an unsteady glottal flow. The nonlinear hydrodynamic equations for a compressible viscous fluid were integrated using MacCormack's difference scheme.

The existence of the FVFs increases the amplitude of pressure fluctuation at the glottis and faraway from the glottis. These increases are due to the interaction of the flow with the edges of the FVFs. Furthermore, the FVFs give rise to the broadbanding of the pressure spectrum throughout the fluid domain. In conclusion, the FVFs have a profound effect on the generation of broadband noise components in a speech wave.

It is difficult to correctly estimate the transition of a turbulent glottal flow, because our computational grid numbers, which are determined from a trade-off between numerical accuracy and computation time (approximately two weeks of CPU time for a workstation with an 2.8-GHz Intel Xeon processor), are insufficient to capture very small scale vortices [11]. In addition, under the assumption of a two-dimensional flow field, large-scale vortices of turbulent flow tend to remain in the field, since the vortex stretching mechanism, which causes the energy cascade from larger to smaller scale vortices, is restricted. Therefore, it is possible that large pressure amplitudes in the region downstream of the FVFs are affected by this fluid motion. A more accurate simulation of the three-dimensional turbulent glottal flow could be obtained if the computing power is increased.

ACKNOWLEDGMENTS

This research was supported in part by the Nakatani Electronic Measuring Technology Association of Japan and by a Grant-in-Aid for Young Scientists (B) (No. 18700171) from the Japan Society for the Promotion of Science.

REFERENCES

[1] K. Ishizaka and J. L. Flanagan, "Synthesis of voiced sounds from a two-mass model of the vocal cords," *Bell Syst. Tech. J.*, **51**, 1233–1268 (1972).
[2] B. H. Story and I. R. Titze, "Voice simulation with a body-cover model of the vocal folds," *J. Acoust. Soc. Am.*, **97**, 1249–1260 (1995).
[3] S. Adachi and J. Yu, "Two-dimensional model of vocal fold vibration for sound synthesis of voice and soprano singing," *J. Acoust. Soc. Am.*, **117**, 3213–3224 (2005).
[4] F. Alipour and R. C. Scherer, "Pressure and velocity profiles in a static mechanical hemilarynx model," *J. Acoust. Soc. Am.*, **112**, 2996–3003 (2002).
[5] G. C. J. Hofmans, G. Groot, M. Ranucci, G. Graziani and A. Hirschberg, "Unsteady flow through *in-vitro* models of the glottis," *J. Acoust. Soc. Am.*, **113**, 1658–1675 (2003).
[6] X. Pelorson, A. Hirschberg, A. P. J. Wijnands and H. Bailliet, "Description of the flow through *in-vivo* models of the glottis during phonation," *Acta Acustica*, **3**, 191–202 (1995).
[7] Z. Zhang, L. Morgeau and S. H. Frankel, "Broadband sound generation by confined turbulent jets," *J. Acoust. Soc. Am.*, **112**, 677–689 (2002).
[8] H. Iijima, N. Miki and N. Nagai, "Glottal impedance based on a finite element analysis of two-dimensional unsteady viscous flow in a static glottis," *IEEE Trans. Signal Process.*, **40**, 2125–2135 (1992).
[9] J. Liljencrants, "Numerical simulations of the glottal flow," *STL-QPSR*, 1/1989, 69–74 (1989).
[10] D. Shinwari, R. C. Scherer, K. J. DeWitt and A. A. Afjeh, "Flow visualization and pressure distributions in a model of the glottis with a symmetric and oblique divergent angle of 10 degrees," *J. Acoust. Soc. Am.*, **113**, 487–497 (2003).
[11] H. Nomura and T. Funada, "Numerical simulation of unsteady flow through the rigid glottis," *Acoust. Sci. & Tech.*, **27**, 154–162 (2006).
[12] C. Zhang, W. Zhao, S. H. Frankel and L. Mongeau, "Computational aeroacoustics of phonation, Part II: Effects of flow parameters and ventricular folds," *J. Acoust. Soc. Am.*, **112**, 2147–2154 (2002).
[13] H. Tennekes and J. L. Lumley, *A First Course in Turbulence* (MIT Press., Cambridge, Mass., 1972), Sect. 8.2, pp. 256–261.
[14] R. C. Scherer, I. R. Titze and J. F. Curtis, "Pressure-flow relationships in two models of the larynx having rectangular glottal shapes," *J. Acoust. Soc. Am.*, **73**, 668–676 (1983).
[15] X. Pelorson, A. Hirschberg, R. R. van Hassel and A. P. Wijnanads, "Theoretical and experimental study of quasisteady-flow separation within the glottal during phonation. Application to a modified two-mass model," *J. Acoust. Soc. Am.*, **96**, 3416–3431 (1994).
[16] J. C. Tannehill, D. A. Anderson and R. H. Pletcher, *Computational Fluid Mechanics and Heat Transfer*, 2nd ed. (Taylar & Francis, Washington DC, 1997), Sect. 5.1, pp. 249–271.
[17] E. Turkel, "On the practical use of high-order methods for hyperbolic systems," *J. Comput. Phys.*, **35**, 319–340 (1980).
[18] T. J. Poinsot and S. K. Lele, "Boundary conditions for direct simulations of compressible viscous flows," *J. Comput. Phys.*, **101**, 104–129 (1992).
[19] R. C. Scherer, D. Shinwari, K. J. De Witt, C. Zhang, B. R. Kucinschi and A. A. Afjeh, "Intraglottal pressure distributions for a symmetric and oblique glottis with a uniform duct (L)," *J. Acoust. Soc. Am.*, **112**, 1253–1256 (2002).
[20] J. C. Hardin, "Acoustic sources in the low Mach number turbulent boundary layer," *J. Acoust. Soc. Am.*, **90**, 1020–1031 (1991).
[21] C. H. Shadle, "The acoustics of fricative consonants," *RLE Tech. Rep.*, No. 506 (1985).

APPENDIX

The width of the larynx is described by the function $w_{\mathrm{L}}(z)$. On the basis of the models of Zhang *et al.* [12] and Scherer *et al.* [14], the larynx shape function of a model with FVFs is written as

$$w_{\mathrm{L}}(z) = w_{\mathrm{L1}}(z) + w_{\mathrm{L2}}(z), \tag{A·1}$$

$$w_{\mathrm{L1}}(z) = \frac{1}{2}\{A_1 + A_2 + (A_1 - A_2)\tanh s(z)\}, \tag{A·2}$$

$$w_{\mathrm{L2}}(z) = \begin{cases} 0 & \text{for } z < H_{\mathrm{FVF}} - \Delta H_{\mathrm{FVF1}}, \\ w_{\mathrm{L21}}(z) & \text{for } H_{\mathrm{FVF}} - \Delta H_{\mathrm{FVF1}} \le z < H_{\mathrm{FVF}}, \\ w_{\mathrm{L22}}(z) & \text{for } z \ge H_{\mathrm{FVF}}, \end{cases} \tag{A·3}$$

where

$$\left.\begin{aligned} &A_1 = W_{\mathrm{sub}},\ A_2 = G_{\mathrm{TVF}}, \\ &s(z) = a_-|z + c_-| - \frac{b_-}{|z + c_-|}, \end{aligned}\right\} \quad \text{for } z \le 0\,\mathrm{mm},$$

$$\left.\begin{aligned} &A_1 = W_{\mathrm{VL}},\ A_2 = G_{\mathrm{TVF}}, \\ &s(z) = a_+|z| - \frac{b_+}{|z|}, \end{aligned}\right\} \quad \text{for } z > 0\,\mathrm{mm}, \qquad \text{(A·4)}$$

$$w_{\mathrm{L21}}(z) = (G_{\mathrm{FVF}} - W_{\mathrm{VL}})\left\{1 + \cos\left(\pi \frac{z - H_{\mathrm{FVF}}}{\Delta H_{\mathrm{FVF1}}}\right)\right\}, \qquad \text{(A·5)}$$

$$w_{\mathrm{L22}}(z) = W_{\mathrm{VT}} - W_{\mathrm{VL}} + (G_{\mathrm{FVF}} - W_{\mathrm{VT}}) \exp\left\{-\frac{1}{2}\left(\frac{z - H_{\mathrm{FVF}}}{\Delta H_{\mathrm{FVF2}}}\right)^2\right\}, \qquad \text{(A·6)}$$

$\Delta H_{\mathrm{FVF1}} = 3.8\,\mathrm{mm}$, $\Delta H_{\mathrm{FVF2}} = 3.0\,\mathrm{mm}$, $a_- = 0.15\,\mathrm{mm}^{-1}$, $b_- = 6.0\,\mathrm{mm}$, $c_- = 0.4\,\mathrm{mm}$, $a_+ = 0.85\,\mathrm{mm}^{-1}$, and $b_+ = 2.0$ mm.

The larynx shape function of the model without the FVFs is written as

$$w_{\mathrm{L}}(z) = w_{\mathrm{L1}}(z), \qquad \text{(A·7)}$$

where $A_1 = W_{\mathrm{VT}}$ for $z > 0\,\mathrm{mm}$, and $a_+ = 0.35\,\mathrm{mm}^{-1}$. Other equations and parameters are the same as those of the model with the FVFs.